渦のつなぎかえの数値シミュレーション : スペクトル法を用いて(ナビエ・ストークス方程式の数値解)

AUTHOR(S):

木田, 重雄; 高岡, 正憲

CITATION:

木田, 重雄 ...[et al]. 渦のつなぎかえの数値シミュレーション : スペクトル法を用いて(ナビエ・ストークス方程式の数値解). 数理解析研究所講究録 1989, 677: 210-219

ISSUE DATE:

1989-01

URL:

http://hdl.handle.net/2433/101014

数理解析研究所講究録
677巻 1989年 190-209

On the Use of Rotational Form in Large Eddy Simulation of Turbulent Channel Flow

Kiyosi HORIUTI

Institute of Industrial Science, University of Tokyo,
7-22-1, Roppongi, Minato-ku, Tokyo 106

Abstract

Fully developed turbulent channel flow is numerically studied by using large eddy simulation (LES) incorporated with the Fourier- finite difference method. A prominent feature of this paper lies in the use of the conservative form of Arakawa type for the convective terms in the Navier-Stokes equations, instead of the rotational form. The results obtained are compared with earlier ones by Moin and Kim [1] based on the latter form. Noticeable differences are found in quantities such as turbulence intensities, two point correlations, etc. The difference is most prominent in the balance of the grid scale portion of the turbulent shear stress. The present results agree qualitatively well with the recent direct simulation of a mildly curved channel flow by Moser and Moin [2] using the Fourier- Chebyshev polynomials expansions. An estimate is made of the error inherent in the rotational form combined with the second-order central finite difference method.

1. Introduction

In the design of numerical schemes, it is well known that the integral constraints on quadratic quantities, such as the conservation of mean energy etc., are quite important to make the computation stable in long-term numerical integrations [3]. Therefore, the conservative form of Arakawa type [4] or the rotational form [5] is widely used for the convective terms in the Navier-Stokes equations. In the present paper, we refer to the conservative form of Arakawa type in primitive variables as the Arakawa form. The rotational form is useful because it preserves mean vorticity, helicity, enstrophy etc. in addition to mean momentum and energy in the absence of external forces and viscous dissipation. The Arakawa form , however, generally preserves only mean momentum and energy. As a matter of fact, the rotational form has been successfully used when combined with Chebyshev polynomials expansion as in [2] .

In the present study, a fully developed turbulent channel flow is numerically studied by using LES with the Fourier- finite difference method. The numerical scheme employed here is basically the same as in [1] and essentially a spectral version of the previous computation [6] in which all partial differential operators were approximated by the finite difference method. The essential point is in the choice of the approximation method for the convective terms in the Navier-Stokes equations and the residual stress model [7] , [1] . In [1] , the convective terms were approximated by using the rotational form. On the other hand, in the present study they are approximated by the Arakawa form and the residual stress model is not employed, unlike [1] . Comparison with [1] and the Fourier - Chebyshev computation in [2] are made and noteworthy differences are found, especially in the balance of GS

portion of turbulent shear stress. It is shown that large truncation errors can occur in the vicinity of the walls when the rotational form is used and the normal derivatives are approximated with the second-order central finite difference method. For details, see [8] .

2. Governing Equations

We consider an incompressible channel flow whose time evolution is governed by the Navier-Stokes and continuity equations for the velocity components u_i (i=1,2,3) and the pressure p :

$$\frac{\partial u_i}{\partial t} + \frac{\partial}{\partial x_j}(u_i u_j) = -\frac{\partial p}{\partial x_i} + \frac{1}{Re}\nabla^2 u_i + 2\,\delta_{i1} \quad , \tag{1}$$

$$\frac{\partial u_i}{\partial x_i} = 0 \quad . \tag{2}$$

Here i,j=1,2,3 correspond to x,y,z, respectively, where x is in the downstream direction, y is in the spanwise direction parallel to the walls, z is in the direction normal to the walls, and δ_{ij} is the Kronecker delta symbol. Occasionally, u_i (i=1,2,3) are denoted by u,v,w, respectively. The flow is driven by the mean pressure gradient. All variables have been made dimensionless by means of the channel width H and the friction velocity u^* [$=(\tau/\rho_0)^{1/2}$; the quantity τ is the wall stress and ρ_0 the density which is assumed constant] . Re is the Reynolds number defined by u^*H/ν (ν is the kinematic viscosity) and Rc represents the Reynolds number defined in terms of the center-plane velocity Uc and H. Moreover, the horizontal average of a quantity is denoted by the angular brackets $\langle\cdot\rangle$, the deviation from the horizontal average by $(\cdot)'$, and the length in wall units by $(\cdot)_+$. The summation convention is used for repeated subscripts.

If f is a function containing all the scales, we define the GS component of f by the convolution of f with a filter function $G_i(x_i,x_i')$ [9] :

$$\overline{f}(x_1,x_2,x_3) = \int_D \prod_{i=1}^{3} G_i(x_i,x_i')\, f(x_1',x_2',x_3')\, dx_1' dx_2' dx_3' . \tag{3}$$

In the present study, the Gaussian filter is used as G_i(i=1,2) in homogeneous directions and the top-hat filter is used as G_3 in the z direction. These filters are selected in the same manner as in [1] . Along with this filtering procedure, the velocity field u_i and the pressure p are decomposed into GS and SGS components as

$$u_i = \overline{u}_i + u_i' \quad , \quad p = \overline{p} + p' \quad . \tag{4}$$

Applying the filtering to equations (1) and (2), we get the following filtered momentum and continuity equations:

$$\frac{\partial \overline{u}_i}{\partial t} + \frac{\partial}{\partial x_j}\overline{u_i u_j} = -\frac{\partial \overline{p}}{\partial x_i} + \frac{1}{Re}\nabla^2 \overline{u}_i + 2\,\delta_{i1} \quad , \tag{5}$$

$$\frac{\partial \overline{u}_i}{\partial x_i} = 0 \quad . \tag{6}$$

Nonlinear terms in eq.(5) are expressed as follows.

$$\overline{u_i u_j} = \overline{u}_i \overline{u}_j + \overline{u}_i' u_j' + u_i' \overline{u}_j' + u_i' u_j' . \tag{7}$$

In this study, the correlations between GS and SGS variables, namely, the second and third terms of (7) are neglected, and the terms with double bars in the x and y directions are explicitly

calculated. The Leonard term arising in the z direction [9] is represented by the truncation error of the second-order central finite difference scheme, because the truncation error is of the same form and order as the Leonard term [1] .

To proceed further, the SGS Reynolds stress $\overline{u_i' u_j'}$ must be modeled in terms of the filtered variables. The method of evaluation used here introduces the SGS eddy coefficient :

$$\overline{u_i' u_j'} - \frac{1}{3}\delta_{ij}\overline{u_l' u_l'} = -\nu_e\left(\frac{\partial \bar{u}_i}{\partial x_j} + \frac{\partial \bar{u}_j}{\partial x_i}\right) , \tag{8}$$

where ν_e is the SGS eddy coefficient. In the present study, the Smagorinsky model [10] is used for ν_e :

$$\nu_e=(c\Delta)^2 \left[\frac{1}{2} e_{ij} e_{ij} \right]^{1/2} , \quad e_{ij} = \frac{\partial \bar{u}_i}{\partial x_j} + \frac{\partial \bar{u}_j}{\partial x_i} . \tag{9}$$

In these expressions, Δ is the representative grid interval $\Delta=(\Delta x\Delta y\Delta z)^{1/3}$, $\Delta x, \Delta y, \Delta z$ denote the computational mesh size in the x, y, z directions, respectively and c is a dimensionless constant. This model may be derived by the use of a statistical approach [11] , and c is chosen equal to 0.1 by computer optimization as in [12] . In order to make (9) compatible with the noslip boundary condition, Δ is multiplied by the damping function of Van Driest type $1-\exp(-z_+/A_+)$ with $A_+=25$ [13] . The Smagorinsky model also can be extended to the modeling of one-equation type(see [7] , [14] , [15]).

In [7] and [1] , the eddy viscosity representation (8) is split into two parts, i.e. homogeneous and inhomogeneous parts as

$$\overline{u_i' u_j'} - \frac{1}{3}\delta_{ij}\overline{u_l' u_l'} = -\nu_e(e_{ij}-\langle e_{ij}\rangle) - \nu_e^* \langle e_{ij}\rangle, \tag{10}$$

which is usually named the residual stress model. In the expression above, ν_e is given by the Smagorinsky model (9) with e_{ij} simply replaced by $e_{ij}-\langle e_{ij}\rangle$. In the inhomogeneous part, ν_e^* is given as follows :

$$\nu_e^* = c^*(D\Delta y)^2 \left[\frac{1}{2} \langle e_{ij}\rangle \langle e_{ij}\rangle \right]^{1/2} , \tag{11}$$

where c^* was chosen equal to 0.065 and D is another type of damping function [1] .

In the present study, the residual stress model is not used owing to the following reason; The inhomogeneous part ν_e^* is what is called the eddy viscosity of mixing length type, which is based on the assumption that the energy production balances with the dissipation in the mean scale. This assumption does not always hold in ducts and external flows, and there seems to be no systematic way of modeling ν_e^* in such flows, at present. The use of (10) may impede the wide application of LES. Therefore, we prefer to avoid the use of models of residual stress type. The necessity of the use of residual stress model in [1] will be discussed in detail in SECTION 5.

For later convenience, we give the energy budget for the GS portion of turbulent energy $\langle \bar{u}_i'' \bar{u}_i'' \rangle /2$ (i=1,2,3 and no summation rule is applied to i):

$$\frac{\partial\langle \bar{u}_i''^2\rangle}{\partial t} = -\frac{1}{2}\delta_{i1}\langle \bar{u}''\bar{w}\rangle\frac{\partial\langle \bar{u}\rangle}{\partial z} - \frac{\partial}{\partial z}\langle \bar{w}\,\bar{u}_i''^2\rangle \tag{12}$$

$$- 2\langle(\nu_e+\frac{1}{Re})\frac{\partial \bar{u}_i''}{\partial x_j}\frac{\partial \bar{u}_i''}{\partial x_j}\rangle - 2\langle \bar{u}_i''\frac{\partial \bar{p}}{\partial x_i}\rangle + \frac{\partial}{\partial z}\langle(\nu_e+\frac{1}{Re})\frac{\partial \bar{u}_i''^2}{\partial z}\rangle$$

$$- 2\langle \bar{u}_i'' \frac{\partial}{\partial x_j}(\overline{\bar{u}_i\bar{u}_j} - \bar{u}_i\bar{u}_j)\rangle \quad .$$

Similarly, the governing equation for the GS portion of turbulent shear stress is expressed as :

$$\frac{\partial\langle \bar{u}''\bar{w}\rangle}{\partial t} = -\langle\bar{w}^2\rangle\frac{\partial\langle\bar{u}\rangle}{\partial z} - \frac{\partial}{\partial z}\langle \bar{u}''\bar{w}^2\rangle - 2\langle(\nu_e + \frac{1}{Re})\frac{\partial \bar{u}''}{\partial x_j}\frac{\partial \bar{w}}{\partial x_j}$$

$$\rangle - \langle \bar{u}''\frac{\partial \bar{p}}{\partial z} + \bar{w}\frac{\partial \bar{p}}{\partial x}\rangle + \frac{\partial}{\partial z}\langle(\nu_e + \frac{1}{Re})\frac{\partial \bar{u}''\bar{w}}{\partial z}\rangle \qquad (13)$$

$$- \langle \bar{u}''\frac{\partial}{\partial x_j}(\overline{\bar{u}_3\bar{u}_j} - \bar{u}_3\bar{u}_j) + \bar{w}\frac{\partial}{\partial x_j}(\overline{\bar{u}_1\bar{u}_j} - \bar{u}_1\bar{u}_j)\rangle \quad .$$

Each term on the right-hand side of (12) and (13) is called the GS production, convection, dissipation, velocity pressure gradient, diffusion and cascade, respectively.

3. Numerical Method

3.1 Numerical approximations

Eq. (5) can be recast into the form that

$$\frac{\partial \bar{u}_i}{\partial t} + \frac{\partial}{\partial x_j}(\overline{\bar{u}_i\,\bar{u}_j}) + \frac{\partial \bar{p}}{\partial x_i} - \frac{\partial\langle\nu_e\rangle}{\partial x_j}\left(\frac{\partial \bar{u}_i}{\partial x_j} + \frac{\partial \bar{u}_j}{\partial x_i}\right) \qquad (14)$$

$$- \frac{\partial}{\partial x_j}\left[\nu_e''\left(\frac{\partial \bar{u}_i}{\partial x_j} + \frac{\partial \bar{u}_j}{\partial x_i}\right)\right] - 2\,\delta_{i1} = \left(\langle\nu_e\rangle + \frac{1}{Re}\right)\nabla^2\bar{u}_i,$$

where the horizontally averaged part of the turbulent viscous terms and its deviation are treated separately. In numerically discretizing eq. (14) in space, the velocity and pressure are represented in the form of the Discrete-Fourier expansion in the downstream and spanwise directions as

$$\bar{u}_{p,q,k} = \sum_{l=-NX/2}^{NX/2-1}\sum_{m=-NY/2}^{NY/2-1}\tilde{u}_{l,m,k}\exp\left(2\pi\sqrt{-1}\left(\frac{pl}{NX} + \frac{qm}{NY}\right)\right) \quad , \qquad (15)$$

where $\sqrt{-1}$ is the imaginary unit, p,q,k are indices of grid positions in the x,y and z directions, respectively, and NX,NY are the numbers of grid points in the x, y directions , respectively. The vertical length is divided into NZ intervals. For the efficiency of computation, the z coordinate is stretched in the hyper tangent profile as

$$z_k = \frac{1}{2}(\tanh(c_0\xi_k)/a + 1) \quad (k=1,NZ), \qquad (16)$$

where z_k is the coordinate of the k-th grid point in the z direction, $c_0=\log((1+a)/(1-a))/2$, $\xi_k=-1+2(k-1)\,\Delta\xi$ and $\Delta\xi=1/(NZ-1)$. The stretching parameter a is selected equal to 0.98346 as in [1] . In discretizing (14) in time, the terms on the right-hand side are approximated by the implicit scheme of Crank-Nicolson type to avoid the use of prohibitively small time intervals, whereas the explicit scheme of Adams- Bashforth type is used for the remaining terms. As stated in SECTION 1, the essential point in the numerical scheme in the present study exists in the choice of an approximation form for the convective terms in the Navier-Stokes eqs. To use the Arakawa form, a regular mesh system is adopted, and all velocity components and pressure are defined at grid points z_k , as given by (16), and both the momentum and continuity equations are enforced at z_k . This grid system eventually leads to the timewise and meshwise

oscillatory solution of $\bar{p}$. This fact led [1] to adopt a staggered grid system. There, the mesh system is staggered only in the z direction. Namely the velocity is defined at z_k and the pressure is defined at $(z_k+z_{k+1})/2$. The momentum equations are enforced at z_k, whereas the continuity equations are enforced at $(z_k+z_{k+1})/2$. In the present study, the Adams-Bashforth method is applied to the pressure gradient terms to avoid oscillations in $\bar{p}$. Thus, we get linear coupled equations for $\bar{u}_i^{n+1}$ and $\bar{p}^n$ as

$$\left(\langle \nu_e \rangle^n + \frac{1}{Re} \right) \nabla^2 \bar{u}_i^{n+1} - 2 \frac{\bar{u}_i^{n+1}}{\Delta t} - 3 \frac{\partial \bar{p}^n}{\partial x_i} \tag{17}$$

$$= - \left(\langle \nu_e \rangle^n + \frac{1}{Re} \right) \nabla^2 \bar{u}_i^n - 2 \frac{\bar{u}_i^n}{\Delta t} - \frac{\partial \bar{p}^{n-1}}{\partial x_i} + d_i \quad ,$$

$$\frac{\partial \bar{u}_i^{n+1}}{\partial x_i} = 0 \quad , \tag{18}$$

where superscript n denotes the time step and d_i consists of the remaining terms. To avoid the iteration procedure, $\langle \nu_e \rangle$ is evaluated at the nth time step. Consequently, eqs. (17) and (18) are solved as a system of coupled equations as in [1] , [5] . Partial differential operators in the z direction are approximated with the second-order central finite difference as

$$\frac{\partial u}{\partial z} \sim \frac{u_{p,q,k+1} - u_{p,q,k-1}}{h_{k+1}+h_k} \quad , \tag{19}$$

$$\frac{\partial^2 u}{\partial z^2} \sim 2\left(\frac{u_{p,q,k-1}}{(h_{k+1}+h_k)h_k} - \frac{u_{p,q,k}}{h_{k+1}\, h_k} + \frac{u_{p,q,k+1}}{(h_{k+1}+h_k)h_{k+1}} \right) ,$$

where $h_k = z_k - z_{k-1}$. Partial differential operators in the x and y directions are approximated by a pseudospectral method.

A system of linear coupled difference equations for every pair of wavenumbers (k_x', k_y') is obtained by inserting the expansion (15) to eqs. (17) and (18); namely

$$L_k \, q_{k-1} + M_k \, q_k + U_k \, q_{k+1} = g_k \qquad (k=2, NZ-1) , \tag{20}$$

where L_k, M_k and U_k are 4 x 4 matrices , $q_k = (\tilde{u}_k, \tilde{v}_k, \tilde{w}_k, \tilde{p}_k)^t$ and the right-hand side of (17) is denoted by g_k . (20) can be easily solved by the conventional method for solving block tri-diagonal equations with only $O((NZ-2))$ arithmetic operations.

3.2 Estimate of truncation errors involved in the Arakawa and rotational forms

In this study, two types of approximation method are applied to the convective terms in the Navier-Stokes equations. One is the Arakawa form, and another is the rotational form. In [6] , the Arakawa form

$$\frac{1}{2} \left\{ \frac{\delta}{\delta x_j}(\bar{u}_i \bar{u}_j) + \bar{u}_j \frac{\delta \bar{u}_i}{\delta x_j} + \bar{u}_i \frac{\delta \bar{u}_j}{\delta x_j} \right\} \tag{21}$$

was employed following [12] ($\delta/\delta x_j$ denotes the second-order central finite difference in the j direction). It was found that the Arakawa form works quite well. Moreover we extended the method of [12] to impose the noslip boundary condition on the walls. In the present study, the second-order Arakawa scheme is modified to its spectral version. That is, partial differential operators in the x and y directions are replaced by those in a pseudospectral method. On the other hand, the rotational form of the convective terms can be written as

$$\bar{u}_j\left(\frac{\partial \bar{u}_i}{\partial x_j}-\frac{\partial \bar{u}_j}{\partial x_i}\right) + \frac{1}{2}\frac{\partial}{\partial x_i}(\bar{u}_j\bar{u}_j) \cdot . \tag{22}$$

Here, no summation rule is applied to i and we note that the GS total energy $\bar{u}_j\bar{u}_j/2$ is not added to the pressure. Both the Arakawa and rotational forms preserve mean momentum and energy in the discretized sense.

The major error in the Arakawa form stems from the x component of (21) as

$$\frac{1}{2}\bar{w}\frac{\partial \bar{u}}{\partial z} + \frac{1}{2}\bar{u}\frac{\partial \bar{w}}{\partial z} + \frac{1}{2}\frac{\partial}{\partial z}(\bar{u}\,\bar{w}). \tag{23}$$

On the other hand, the major error in the rotational form comes from the term in the z component of (22) as

$$-\bar{u}\frac{\partial \bar{u}}{\partial z} + \frac{1}{2}\frac{\partial}{\partial z}\bar{u}^2. \tag{24}$$

Eqs. (23), (24) are approximated by using the central finite difference as

$$\frac{1}{2}\bar{w}_k\frac{\bar{u}_{k+1}-\bar{u}_{k-1}}{h_{k+1}+h_k} + \frac{1}{2}\bar{u}_k\frac{\bar{w}_{k+1}-\bar{w}_{k-1}}{h_{k+1}+h_k} + \frac{1}{2}\frac{\bar{w}_{k+1}^2-\bar{w}_{k-1}^2}{h_{k+1}+h_k}, \tag{25}$$

$$-\bar{u}_k\frac{\bar{u}_{k+1}-\bar{u}_{k-1}}{h_{k+1}+h_k} + \frac{1}{2}\frac{\bar{u}_{k+1}^2-\bar{u}_{k-1}^2}{h_{k+1}+h_k}, \tag{26}$$

respectively. By using the Taylor expansion around z_k, we get the error estimate for (24) as

$$(h_{k+1}-h_k)\left(\frac{\partial \bar{u}}{\partial z}\right)^2. \tag{27}$$

Here, the horizontal average of (27) can be written as follows:

$$(h_{k+1}-h_k)\left(\frac{\partial \langle\bar{u}\rangle}{\partial z}\right)^2 + (h_{k+1}-h_k)\left\langle\left(\frac{\partial \bar{u}''}{\partial z}\right)^2\right\rangle. \tag{28}$$

Because $\langle\bar{u}\rangle$ stands linearly in wall units near the walls in turbulent channel flow, the first term in (28) becomes $(h_{k+1}-h_k)Re^2$. In addition, $(h_{k+1}-h_k)$ is estimated as

$$(h_{k+1}-h_k) \sim (\Delta\xi)^2\,\chi(\xi)\ , \tag{29}$$

where

$$\chi(\xi)=\frac{\partial^2 z}{\partial \xi^2} = -c_0^2\frac{\tanh(c_0\xi)}{a\cosh^2(c_0\xi)} \quad .$$

Hence, the estimate of the first term in (28) is given as $\sim(\Delta\xi)^2\,\chi(1)\,Re^2$. This amounts to the order of 10^2 to 10^3 in the current computation. Thus, the term (28) introduces a critical source of error into the right hand side of (20) in the vicinity of the wall, which leads to the spurious solutions of $\bar{p}$ and $\bar{w}$ near the walls, as will be discussed in SECTION 5. Similarly, the corresponding truncation error for (23) is estimated as

$$(h_{k+1}-h_k) < \frac{\partial \bar{u}}{\partial z}\frac{\partial \bar{w}}{\partial z} + \bar{u}\frac{\partial^2 \bar{w}}{\partial z^2} + \bar{w}\frac{\partial^2 \bar{u}}{\partial z^2} >. \tag{30}$$

The limiting slope for the normal velocity in the vicinity of the wall, is zero. Therefore, in the current computation, with the noslip boundary condition on the wall, the error (30) is estimated to be smaller than (28) by the order of 10^3 to 10^4. Thus, no serious error is introduced by using the Arakawa form (21).

3.3 Computed cases

The region to be treated has a streamwise length (L_x) of 3.2 H and a spanwise one (L_y) of 1.6 H. The size of computational domain in the x and y directions must minimize the effect of imposed periodic boundary conditions. The two-point correlation measurements in [16] are used as a criterion. Re is set at 1280 (Rc = 27800).

The initial condition was generated from the interpolation of the data obtained in the previous computation [15] with the number of grid points as 32x32x32. For the details of this computation, see [15] . Computations were done until a statistically steady state was reached, and then further continued to obtain reliable statistical quantities. In all cases shown here, the time interval Δt is set at 0.0005.

The Arakawa form is employed in Case 1. The integration time of Case 1 is 9.85 in non-dimensional time units. The rotational form is used in Case 2. There, the computation is restarted from the intermediate stage of Case 1 (at t=9.6), and the convective terms are switched from the Arakawa form to the rotational form and extended until t= 11.1. Horizontal averaged values are averaged further over the last 3.0 and 1.5 time units in Case 1 and 2, respectively. In SECTIONS 4 and 5, $\langle\cdot\rangle$ indicates horizontal as well as time averaged values.

Computation was done with the HITAC S-810 model 20 system of the Computer Center of the University of Tokyo.

Using flow visualization techniques, several features of the boundary layer flow in the near wall region have been revealed by Kline et al. [17] . The flow was visualized by the time lines of hydrogen bubbles released from a wire. It was found that even when the wire was placed very near the wall, the bubbles did not follow straight trajectories, but rather accumulated into an alternating array of high- and low- speed regions called ' streaks '. The mean spacing of streaks is known to be approximately 100 in wall units. This value can be used as one of indicators of the reliableness of simulated results.

4. Results and Discussion of Case 1.

In this section, we show the results from Case 1. For comparison with previous numerical simulations, we refer to [1] and [2] . In [1] , Fourier series were used with NX=64, NY=128 and finite difference was used in the z-direction with NZ=63. In the present study, NX=NY=64 Fourier series with finite difference in the z direction with NZ=62 are used. Note that the number of grid points employed in the spanwise direction in the present study is half that in [1] . In [2] , NX=NY=128 Fourier series were used with 65 Chebyshev polynomials expansion in the z-direction.

Figure 1 shows the mean streamwise velocity profile obtained in Case 1. This profile approximately fits the curve $\langle \bar{u} \rangle = z_+$ in the vicinity of the wall, and in the logarithmic region approximately fits the curve

$$\langle \bar{u} \rangle = \frac{1}{0.4} \log z_+ + 6.2. \qquad (31)$$

The Karman constant 0.4 obtained is in good agreement with the value determined experimentally in [18] , [19] , but the constant 6.2 is larger than the generally accepted value of 5.0 in [19] , [20] and that in [1] , and close to the value of 5.9 in [21] . The value of 6.2, however, is considerably improved from 7.0 in the computation with 32x32x32 grid points [15] . We note that this constant seems to

be controllable by optimizing a constant c^* in (11) in case of adopting the residual stress model [1] . In the present study, we have abondoned the use of the residual stress model as mentioned in SECTION 2.

Figure 2 plots the profiles of the GS mean Reynolds stress $<\bar{u}''\bar{w}>$ and the total stress

$$<\bar{u}''\bar{w}>-<\nu_e(\frac{\partial\bar{u}}{\partial z}+\frac{\partial\bar{w}}{\partial x})>-\frac{1}{Re}\frac{\partial<\bar{u}>}{\partial z}.$$

The total stress balances the downstream mean pressure gradient, which is plotted by a dashed line in the figure. So, our computations are considered to be statistically in equilibrium.

Figure 3 shows the profiles of the correlation function between the GS streamwise and normal components of fluctuations, $<\bar{u}''\bar{w}>/<\bar{u}''^2>^{1/2}/<\bar{w}^2>^{1/2}$. These profiles agree fairly well with the data in [22] and we find that streamwise and normal fluctuations are highly correlated.

Figure 4 (a) displays GS turbulence intensities in the x,y,z directions from Case 1 and Fig. 4 (b) shows the intensities in the vicinity of the lower wall vs. wall units. For comparison, the computational data in [1] or the experimental measurement in [23] are plotted in the figure. From these figures, we see that the amplitude of $<\bar{u}''^2>^{1/2}$ is larger than in [1] and [23] , and $<\bar{w}^2>^{1/2}$ is slightly larger than in [1] and [23] . We find an appreciable difference in $<\bar{v}^2>^{1/2}$ between the present result and that of [1] : the position of the peak in our case is closer to the wall than that in [1] , and shows better agreement with [23] . The overall agreement with [23] is good.

Figure 5 plots the streamwise two point correlation function $R_{ii}(r_1;z)$ at two locations (z= 0.0128 and 0.0626). $R_{ii}(r_1;z)$ is defined by

$$R_{ii}(r_1;z)=<\bar{u}_i''(x+r_1,y,z)\ \bar{u}_i''(x,y,z)>/<\bar{u}_i''^2(x,y,z)> . \qquad (32)$$

The profiles of $R_{11}(r_1;z)$ at z= 0.055 from [16] and $R_{11}(r_1;z)$ at z= 0.0125 and 0.0605 from [1] are included. We should note that these profiles are obtained at slightly different vertical locations. As found in [1] , for small values of r_1 , the measured correlations in [16] are smaller than the computed results. For larger values of r_1 , it was pointed out in [1] that computed results are smaller than experimental measurements in [16] . The present correlation persists over a longer distance in the downstream direction than in [1] and shows good agreement with the experimental observation that mean streamwise length of streak extends beyond 1000 in wall units [24]

The spanwise two point correlation functions $R_{ii}(r_2;z)$ defined by

$$R_{ii}(r_2;z)=<\bar{u}_i''(x,y,z)\ \bar{u}_i''(x,y+r_2,z)>/<\bar{u}_i''^2(x,y,z)>, \qquad (33)$$

at the same locations as in Fig.5 are plotted in Fig. 6. By using the position of the negative peak closest to the wall in $R_{11}(r_2;z)$, we can estimate the mean spacing of neighbouring streaks as 250, which is considearbly larger than the generally accepted value of 100 in [17] . A similar defect is also reported in [1] . The reason for this discrepancy may be, as pointed out in [1] , that the grid resolution is not sufficient for the Reynolds number considered. Nevertheless, our mean spacing of streaks is found to be very close to that in [1] , in spite of the fact that the number of grid points employed in the spanwise direction is half that in [1] .

Figures 7 (a),(b) and (c) display the budget of the GS portion

of three components of turbulent intensities from Case 1. In the downstream component, the production and dissipation terms are dominant in the central region, but the diffusion term is dominant near the wall. The diffusion term changes sign from positive to negative as we depart from the wall [15]. The balances in both the streamwise and spanwise components are qualitatively the same as in [1], but the peak values of the production and dissipation terms in the streamwise component are larger than in [1]. On the contrary, the GS energy balance in the z direction is qualitatively different from that of [1]. For comparison, the energy balance of the GS normal component from [1] is reproduced in Fig. 7 (d), where only convection, velocity pressure gradient and dissipation terms are plotted. Both in [1] and the present study, the velocity pressure gradient term compensates for the loss in the dissipation term in the central region of the channel. On the other hand, in the vicinity of the wall, the velocity pressure gradient term has a large gain, peaked at $z_+ \sim 10$ in [1]. The convection term makes up for this peak. By contrast, this peak is absent in the present study. Figure 7 (e) plots the corresponding energy balance from a direct simulation of a mildly curved channel flow [2]. Although the contribution of the convection term in the present study is larger than in [2], the result in [2] qualitatively agrees well with the present study. Here, we should refer to the effect of curvature in [2] and the difference in the Reynolds number in [1] and [2]. For the former, in [2], computation was performed at a mild curvature, say $H/(4R) \sim 0.01$ where R denotes a radius of curvature. Therefore, the comparison with the present study will be plausible because the curvature will not affect the results crucially until z_+ is sufficiently large, as pointed out in [2]. Moreover, only the balance in the vicinity of the concave wall is shown in Figs. 7(e) and 8(c), but the balance is remarkably similar on both the convex and concave sides when normalized by local wall units in [2]. For the Reynolds number dependence, the simulation in [2] is done at a relatively lower Reynolds number of 336 compared with 1280 in [1]. Therefore, the large peak of the velocity pressure gradient term in the vicinity of wall in [1] may be attributed to the higher Reynolds number effect.

A more distinctive difference, however, is identified in the balance of the GS portion of turbulent shear stress as follows. Figures 8 (a),(b),(c) display the budget of the GS portion of turbulent shear stress in the present study, [1] and [2], respectively (only production, convection, velocity pressure gradient terms are reproduced in Figs. 8 (b), (c)). In accordance with the large peak of the convection term near the wall in Fig. 7 (d), large peaks can be depicted in both the convection and the velocity pressure gradient terms in [1], whereas these peaks are absent in the present study and [2]. Instead, the production term has a large peak at $z_+ \sim 25$ in the present study and at $z_+ \sim 15$ in [2]. In the central region of the channel, the convection term balances with the production term in [1], whereas the velocity pressure gradient term balances with the production term in both the present study and [2]. This discrepancy will be quite crucial for the modeling of stress equation type. So far no experimental measurement of the budget of turbulent shear stress is available, but the result that the production term has a large peak near the wall in Figs. 8 (a) and (c) is consistent with the experimental observation that the turbulent energy production is maximum at $z_+ \sim 15$. (see [25])

Figure 9 (a) plots the instantaneous contour lines of $\bar{u}''$ in the x-y plane located at $z_+ = 6.4$ and at $t = 9.6$. In Fig. 9, positive

values are contoured by solid lines and negative values by dashed lines. In this figure, an array of highly elongated regions of high-speed fluid $\bar{u}''$ can be discerned, which corresponds to the experimentally observed streaks. However, the mean spacing of streaks in Case 1 is approximately 250 in wall units as estimated by the spanwise correlations. The instantaneous contour lines of $\bar{p}''$ in the x-y plane located at $z_+ = 6.4$ and at $t = 9.6$ are displayed in Fig. 9 (b). With the Adams-Bashforth method for pressure gradient terms, the meshwise oscillations are suppressed as shown in the figure, and the root mean square value of the GS wall pressure fluctuations is about 2.0, which is in fair agreement with the experimental measurement of 2.3 in [26] and the computational result 2.05 in [1].

Time lines from Case 1 are displayed in Fig. 10, where a wire is set parallel to the y-axis at $z_+ = 12.8$. The streaks can be clearly identified in this figure and agreement with experimental observations in [17] is good as in [1].

5. Results and Discussion of Case 2.

In Case 2, the convective terms are switched from the Arakawa form to the rotational form. The mean streamwise velocity profile, the Reynolds stress distribution and turbulence intensities of streamwise component are plotted in Figs. 11, 12 and 13, respectively. As can be found in the figures, GS Reynolds stress and turbulence intensities gradually decayed. Thus the mean streamwise velocity profile returned to the laminar parabolic profile. Therefore, unless we use a residual stress model with the rotational form, the turbulence will die out. It is numerically found that right after the Arakawa form is switched to the rotational form, a source of error introduced by the large truncation error (28) into the right hand side of eq. (20) in the vicinity of the wall induces the spurious solution of $\bar{p}$. As a result, the amplitude of the velocity-pressure gradient term in the normal component of turbulent energy balance, substantially increases. Thus, $\langle \overline{w}^2 \rangle^{1/2}$ appreciably increases. Because the approximation method for the convective terms is designed to preserve mean energy, the net transfer of turbulent energy from the downstream component to the spanwise and normal components is carried out: $\langle \overline{u}''^2 \rangle^{1/2}$ substantially decreases and $\langle \overline{v}^2 \rangle^{1/2}$ slightly increases.

Figure 14 shows the balance of turbulent shear stress. Comparison with Fig. 8 (a) reveals that the velocity pressure gradient term changes its sign from positive to negative and, as a matter of fact, this change occured right after we had switched the Arakawa form to the rotational form. This abrupt change is caused by the large truncation error (28) as in the balance of normal component of turbulent energy. Consequently, the total summation of all terms in the right hand side of (13) turned out to be negative in the lower half of the channel. If we employ the residual stress model with the rotational form, the convection term will compensate for the velocity pressure gradient term as in [1]. Otherwise, the total summation remains negative, which means that the turbulent shear stress decreases with the lapse of time. In order to reach a statistical equilibrium, the total summation should asymptotically approach zero. In keeping the total summation negative, an equilibrium can be accomplished only by setting all terms in the right hand side of (13) to zero. This is why the GS shear stress decayed, as depicted in Fig. 12. The large peak in the production term observed in Case 1 gradually disappeared, and it is totally

absent from Fig. 14. The distributions of velocity pressure gradient and production terms from Case 2 qualitatively agree with those in [1] . It will be interesting to note here that at t=11.1 in Case 2, we switched back to the Arakawa form again, and then the turbulence began to revive.

6. Conclusions

Turbulent plane channel flow is numerically studied using a large eddy simulation combined with the Fourier- finite difference method. Namely, the pseudospectral method is used in the downstream and spanwise directions, while the second-order central finite difference method is applied in the normal direction. The numerical method is basically the same as in [1] , but we have four choices in the combination of the approximation method for the convective terms in the Navier-Stokes equations [i.e. the conservative form of Arakawa type (refered to as "CS" below) or the rotational form (RT)] and the turbulence modeling [i.e. with the residual stress model (RS) or without the residual stress model (NORS)] . In this paper, the citation is limited to the results with a regular grid system. The results with a staggered grid system combined with the combination of RT- NORS have been omitted. The latter computation showed no significant differences from Case 2 of the present study, in which RT-NORS is found to fail. In [1] , RT-RS is employed, and in Case 1 of the present study CS-NORS is used. These two computations, however, showed considerable differences. Among them, the difference in the balance of the grid scale portion of the turbulent shear stress is considerable. Consequently, appreciable differences are found in turbulence intensities and two point correlations. The mean spacing of streaks is estimated as 250 in wall units, which is close to that in [1] , although the number of grid points in the spanwise direction used here is half that in [1] . Comparison with a direct numerical simulation in [2] is made and it is confirmed that the results in the present study are qualitatively consistent with [2] . An analytical estimate of the error in the vicinity of the wall involved in the rotational form combined with the Fourier- finite difference method is made and its conformity with the results in the numerical simulation is shown. Although these errors are absent in case that higher-order schemes or Chebyshev polynomials expansion is used, the truncation error associated with the second-order central finite difference can lead to significantly inaccurate results. Finally, we mention the last combination CS-RS: this combination may be useful to improve the higher constant 6.2 in the mean streamwise velocity profile.

Acknowledgement

The author is grateful to Professor J.H. Ferziger of Stanford University and A. Yoshizawa for valuable comments.

7. References

1. P. Moin and J. Kim, J. Fluid Mech. 118 , 341 (1982).
2. R. D. Moser and P. Moin, NASA Technical Memorandum No. 85974, 1984.
3. N.A. Phillips, Quart. J. Roy. Meteorol. Soc. 82 , 123 (1956).
4. A. Arakawa, J. Comp. Phys. 1 , 119 (1966).
5. D. O. Gottlieb and S. A. Orszag, Numerical Analysis of Spectral Method : Theory and Applications, (NSF-CBMS Monograph No.26, Soc.

Indus. Appl. Math., Philadelphia, 1977).
6. K. Horiuti, Theor. Appl. Mech. 31 , 407 (1982).
7. U. Schumann, J. Comp. Phys. 18 , 376 (1975).
8. K. Horiuti, To appear in J. Comp. Phys. (1986).
9. A. Leonard, Adv. Geophys. 18A , 237 (1974).
10. J. Smagorinsky, S. Manabe, and J. L. Holloway, Mon. Weath. Rev. 93, 727 (1965).
11. A. Yoshizawa, Phys. Fluids 25 , 1532 (1982).
12. J. W. Deardorff, J. Fluid Mech. 41 , 453 (1970).
13. E. R. Van Driest, J. Aero. Sci. 23 , 1007 (1956).
14. A. Yoshizawa and K. Horiuti, J. Phys. Soc. Jpn. 54 , 2834 (1985).
15. K. Horiuti, J. Phys. Soc. Jpn. 54 , 2855 (1985).
16. G. Comte-Bellot, Thesis, University of Grenoble (1963).
17. S. J. Kline, W. C. Reynolds, F. A. Schraub, and P. W. Runstadler, J. Fluid Mech. 30 , 741 (1967).
18. P.S. Klebanoff, NACA Report No. 1247, 1955.
19. A.K.M.F. Hussain and W.C. Reynolds, J. Fluids Engrg. 97 , 568 (1975).
20. H. Tennekes and J.L. Lumley, A First Course in Turbulence (The MIT Press, Cambridge, 1972),p. 149.
21. H. Ecklemann, J. Fluid Mech. 65 , 439 (1974).
22. J. Sabot and G. Comte-Bellot, J. Fluid Mech. 74 , 767 (1976).
23. H. Kreplin and M. Ecklemann, Phys. Fluids 22 , 1233 (1979).
24. R.F. Blackwelder and H. Eckelmann, J. Fluid Mech. 94 , 577 (1979).
25. H.T. Kim, S. J. Kline and W. C. Reynolds, J. Fluid Mech. 50 , 133 (1971).
26. W.W. Willmarth, Ann. Rev. Fluid Mech. 7 , 13 (1975).

Figures

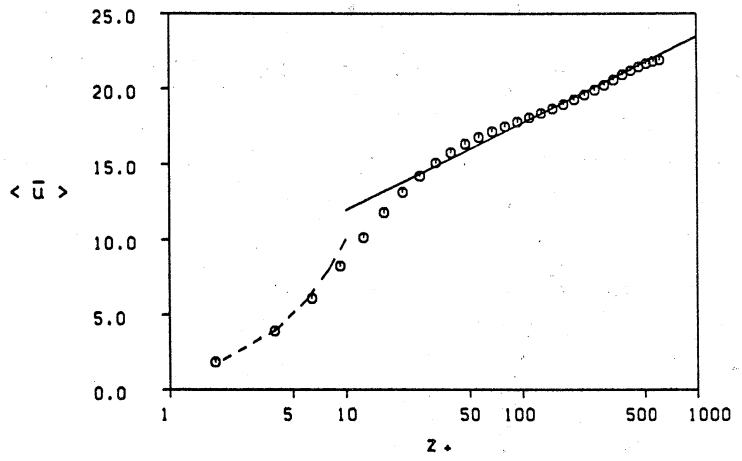

Fig. 1: Mean streamwise velocity profile $\langle \bar{u} \rangle$ from Case 1 ; O , computation; — — — — — —, $\langle \bar{u} \rangle = z_+$; ———— , $\langle \bar{u} \rangle = 1/0.4 \log z_+ + 6.2$.

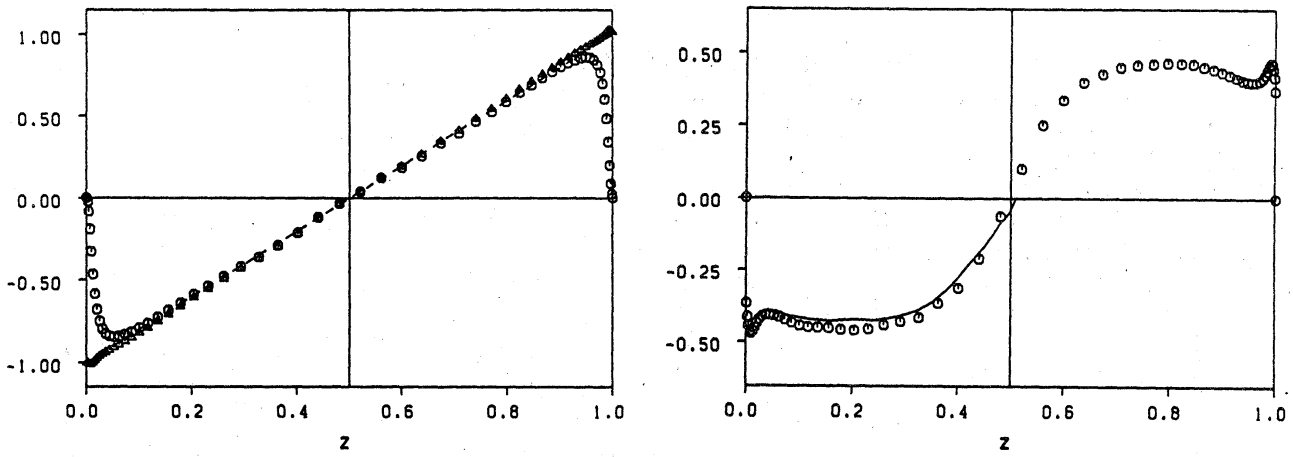

Fig. 2: Mean GS Reynolds stress and the total stress from Case 1 ; O , $\langle \bar{u}'' \bar{w} \rangle$; Δ ,

$$\langle \bar{u}'' \bar{w} \rangle - \langle \nu_e \left(\frac{\partial \bar{u}}{\partial z} + \frac{\partial \bar{w}}{\partial x} \right) \rangle - \frac{1}{Re} \frac{\partial \langle \bar{u} \rangle}{\partial z}.$$

Fig. 3: Correlation coefficient between the GS streamwise and normal components of fluctuations from Case 1 (O); ——————— , experimental data in [22] .

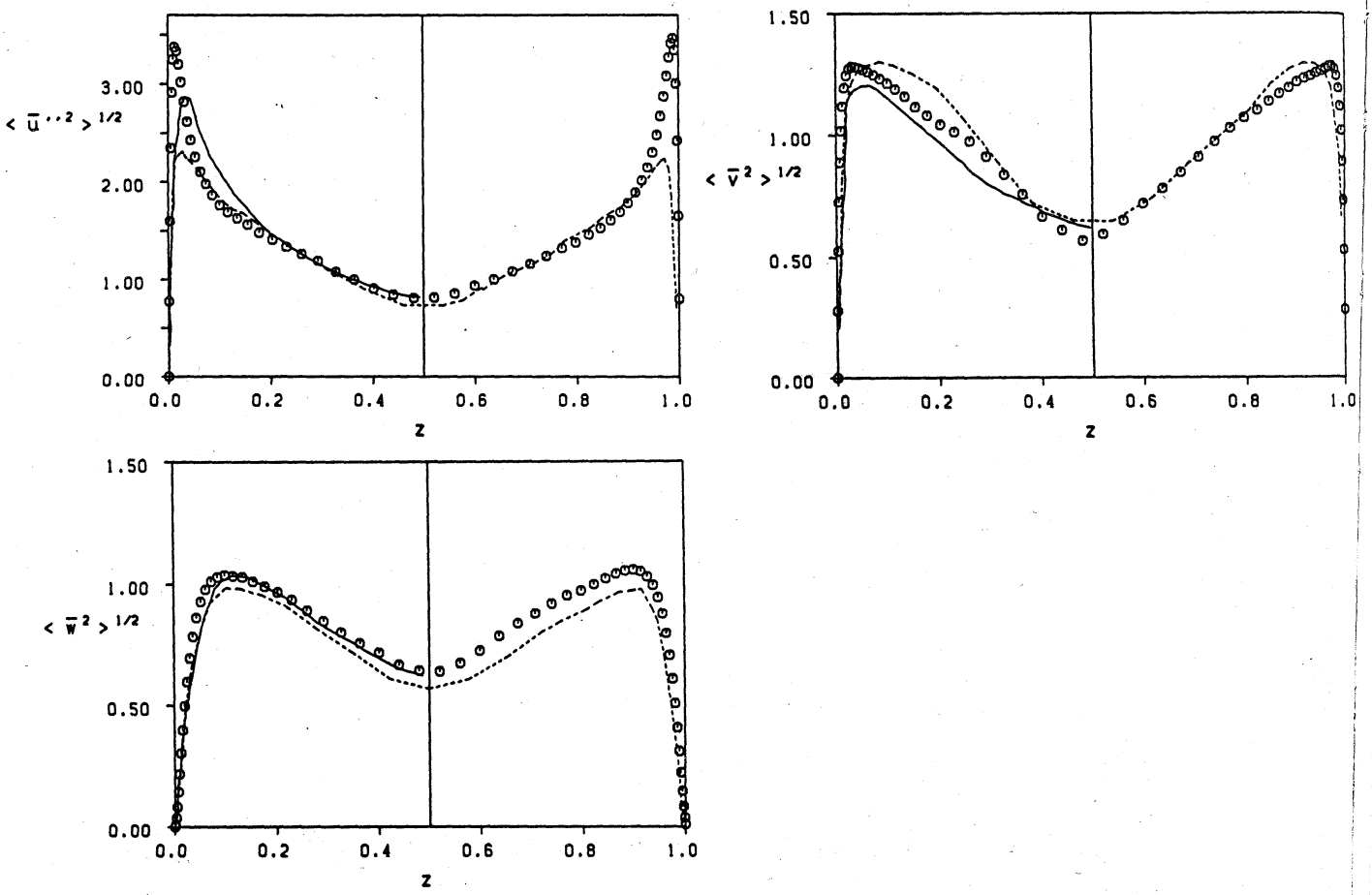

Fig. 4 (a): GS turbulence intensities from Case 1 (O); — — — — — — — , computational data in [1] ; ——————— , experimental data in [23] .

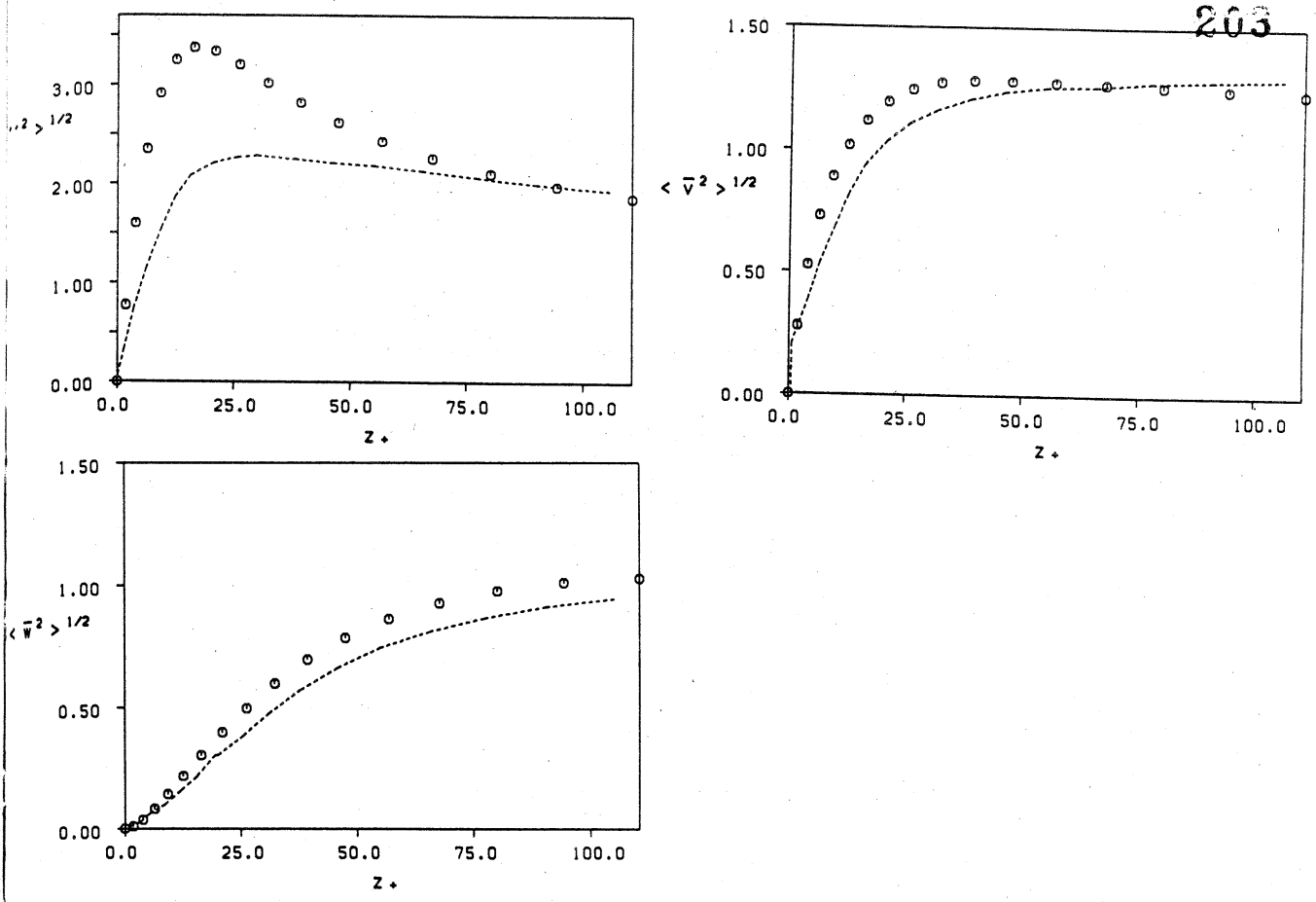

Fig. 4 (b): GS turbulence intensities in the vicinity of the lower wall from Case 1 (O); — — — — — — — , computational data in [1]

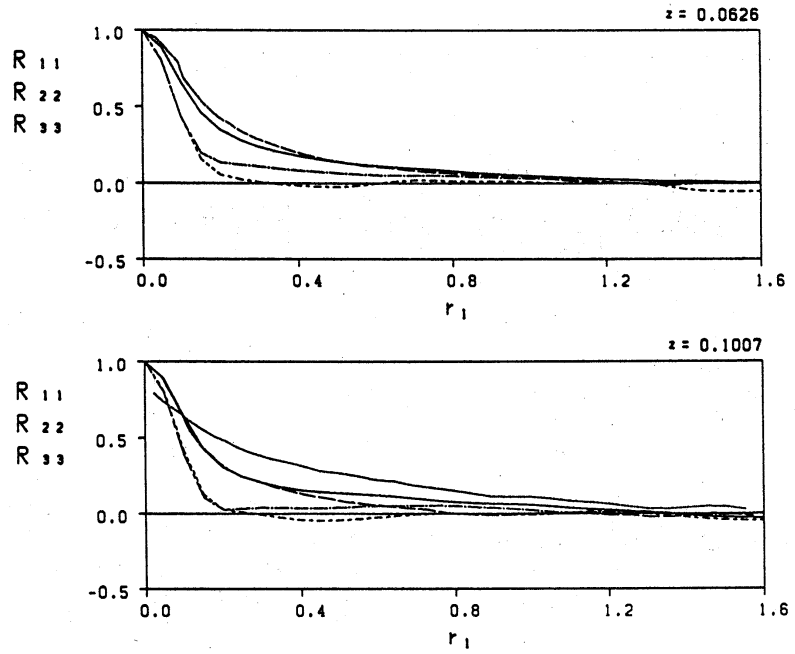

Fig. 5: Streamwise two point correlation function $R_{ii}(r_1;z)$; ——————, R_{11} from Case 1 of the present study; - - - - - - - - - - - - -, R_{22} ; — — — — — — — — — — —, R_{33} ; ····· , experimental data in [16] ; — — — — — — , computational data in [1]

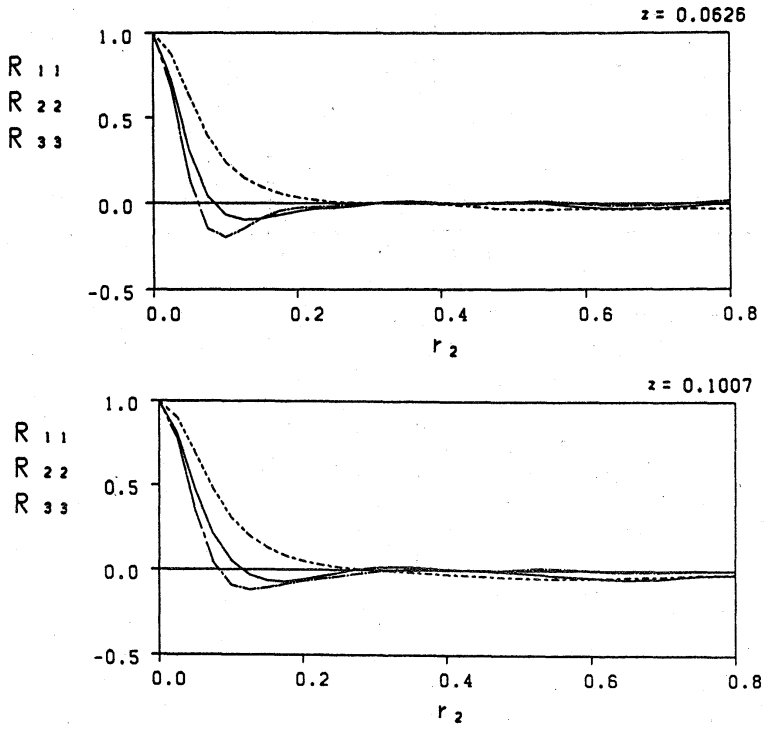

Fig. 6: Spanwise two point correlation function $R_{ii}(r_2;z)$; ——————, R_{11} ; - - - - - - - - - - - , R_{22} ; ——— · ——— · ———, R_{33}

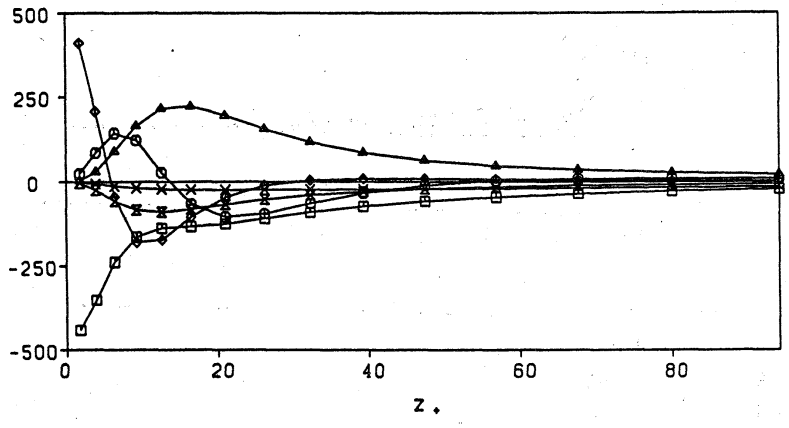

Fig. 7 (a): Balance of ensemble averaged GS portion of the streamwise component of turbulent kinetic energy from Case 1. △ , production ; ○ , convection ; × , velocity pressure gradient ; ◇ , diffusion ; □ , dissipation ; ⧗ , cascade.

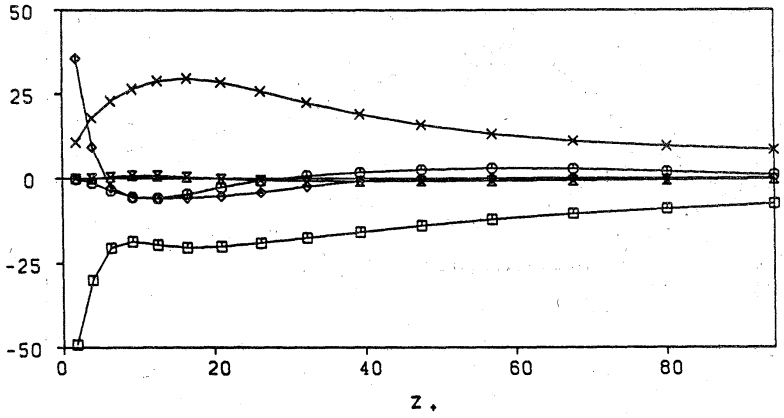

Fig. 7 (b): Balance of GS portion of the spanmwise component of turbulent kinetic energy. See caption of Fig. 7(a) for details.

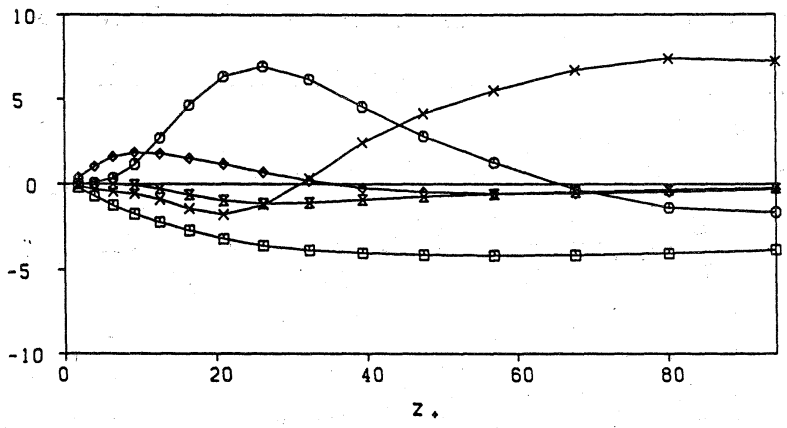

Fig. 7 (c): Balance of GS portion of the normal component of turbulent kinetic energy.

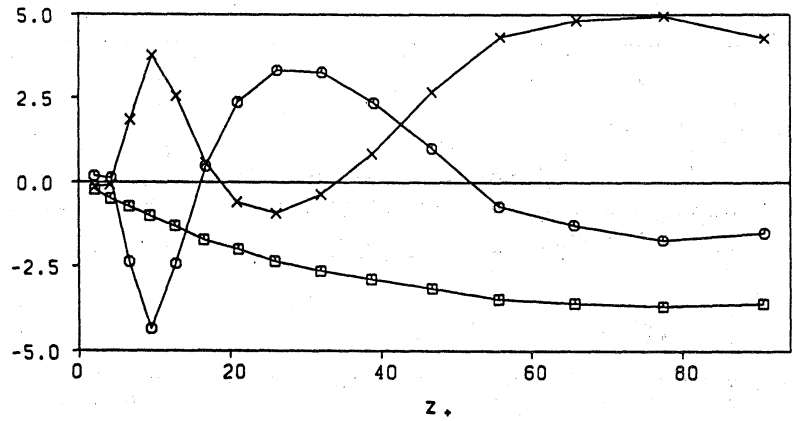

Fig. 7 (d): Balance of GS portion of the normal component of turbulent kinetic energy from previous numerical calculations [1].

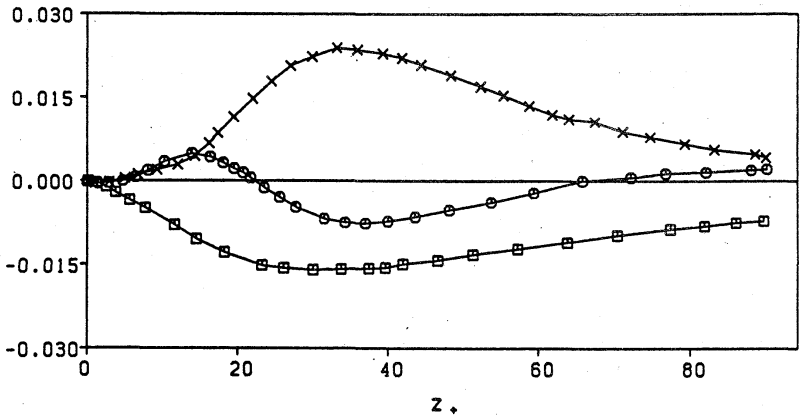

Fig. 7 (e): Balance of GS portion of the normal component of turbulent kinetic energy in the vicinity of concave wall from previous numerical calculations [2]. Note that the positions of markers do not coincide with the Chebyshev collocation points.

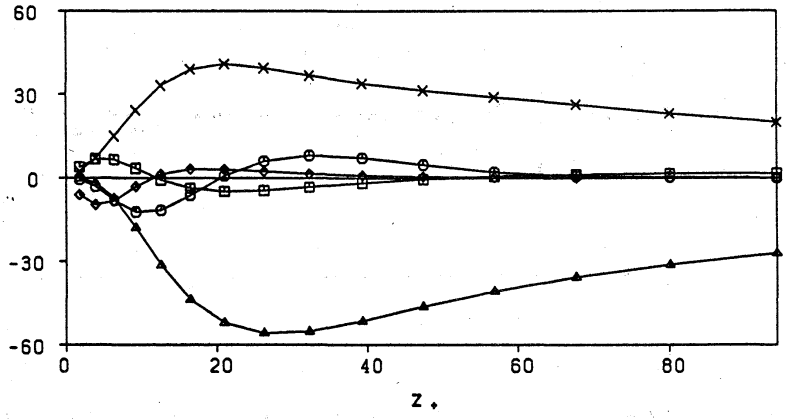

Fig. 8 (a): Balance of ensemble averaged GS portion of turbulent shear stress from Case 1. See caption of Fig. 7(a) for details.

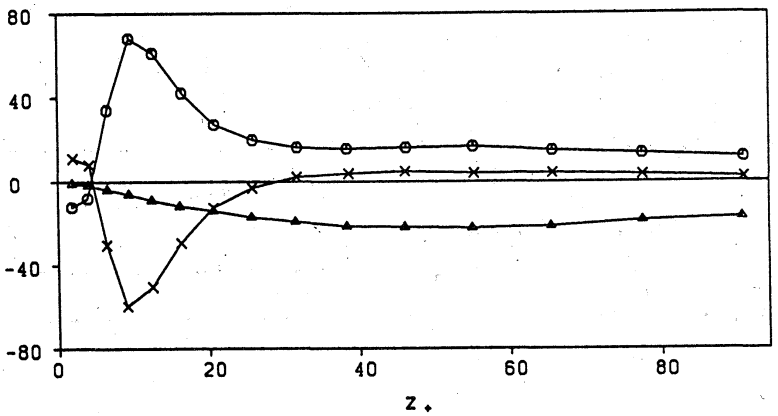

Fig. 8 (b): Balance of GS portion of turbulent shear stress from previous numerical calculations [1].

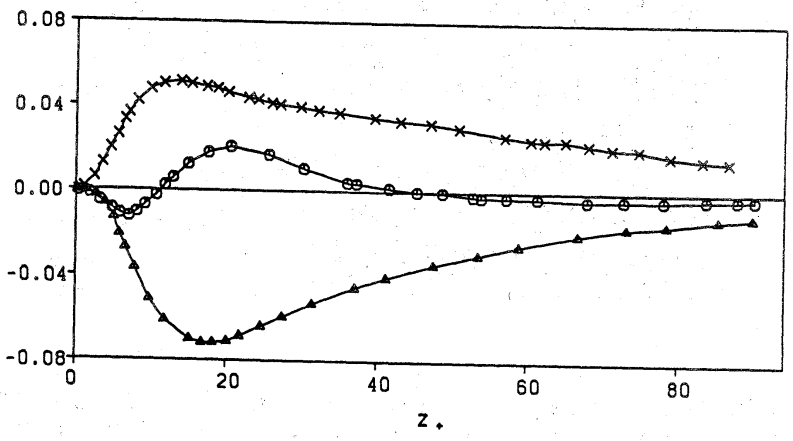

Fig. 8 (c): Balance of GS portion of turbulent shear stress in the vicinity of concave wall in previous numerical calculations [2]. See caption of Fig. 7(a) and (e) for details.

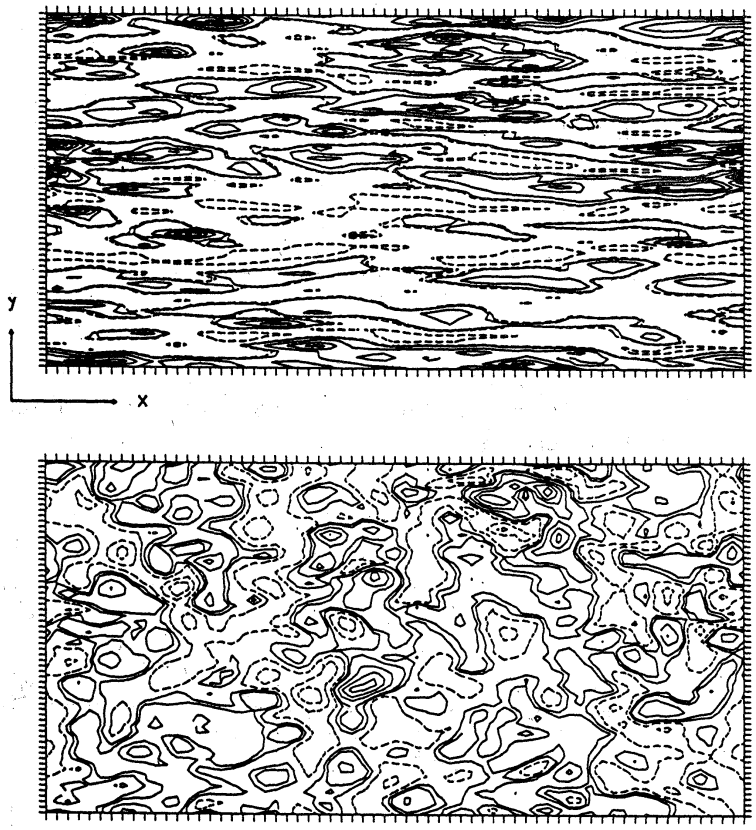

Fig. 9 (a): Contour lines of $\overline{u}''$ in the x–y plane at z_+=6.4, t=9.6 from Case 1.
(b): Contour lines of $\overline{p}''$ in the x–y plane at z_+=6.4, t=9.6 from Case 1.

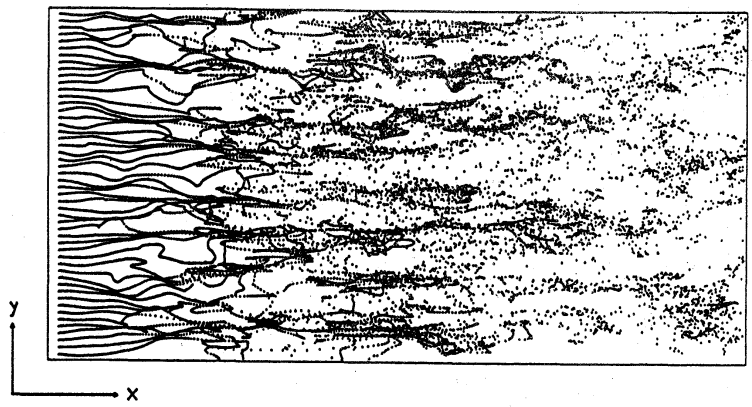

Fig. 10: Top view of streaky structure visualized by passive markers introduced along a horizontal wire set at $z_+ = 12.8$ from Case 1.

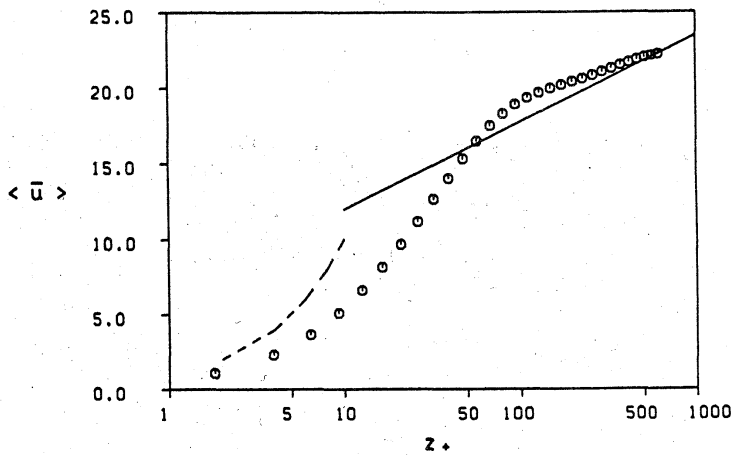

Fig. 11: Mean streamwise velocity profile $\langle \bar{u} \rangle$ from Case 2. See caption of Fig. 1 for details.

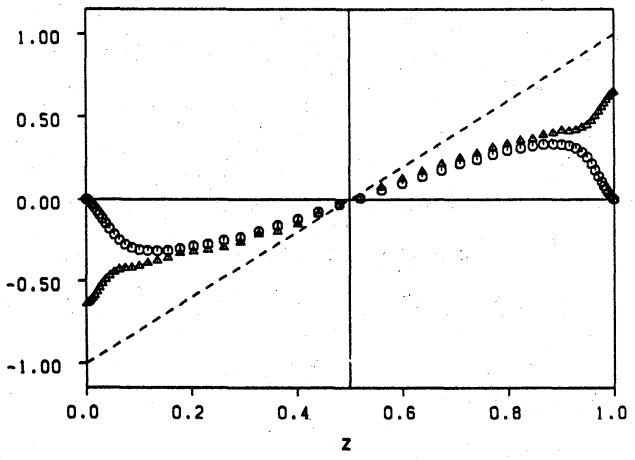

Fig. 12: Mean GS Reynolds stress and the total stress from Case 2 ; O , $\langle \bar{u}' \bar{w}' \rangle$; Δ , The total stress.

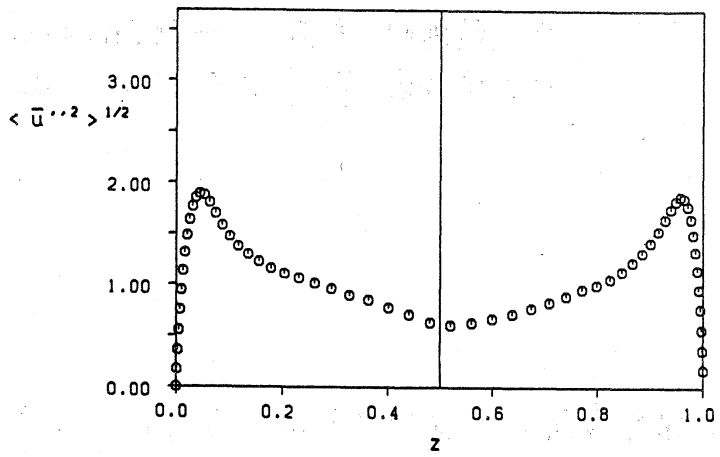

Fig. 13: GS turbulence intensities of streamwise component from Case 2 (O).

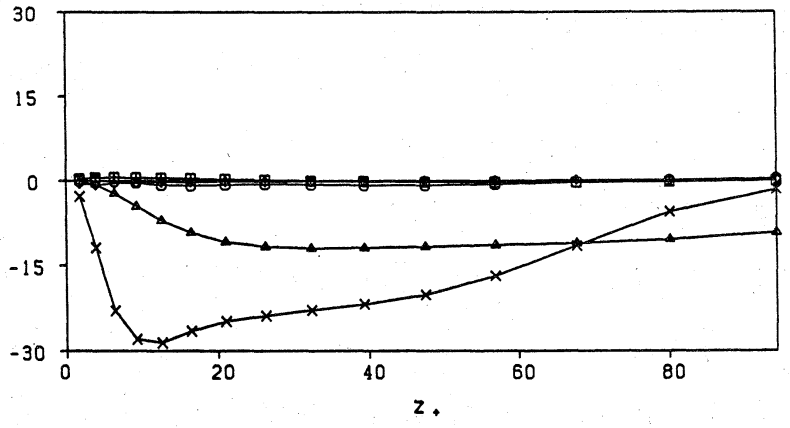

Fig. 14: Balance of ensemble averaged GS portion of turbulent shear stress from Case 2. See caption of Fig. 7(a) for details.